Study of the $\bar{p}d \rightarrow p_s\bar{p}p\pi^-$ Reaction at 5.5 GeV/c

H. BRAUN, D. EVRARD, A. FRIDMAN*, J.-P. GERBER, G. MAURER, A. MICHALON, B. SCHIBY, R. STRUB, C. VOLTOLINI, AND P. CÜER

Laboratoire de Physique Corpusculaire, Centre de Recherches Nucléaires de Strasbourg, Strasbourg, France

(Received 7 April 1970)

Based on 150 000 photographs taken with the 30-in. bubble chamber at the ZGS, we present a study of the $\bar{p}d \rightarrow p_s\bar{p}p\pi^-$ reaction. Important production of $\bar{\Delta}^{--}(1236)$ is observed. The distribution of the momentum transfer between the incident $\bar{p}$ and the final $\bar{\Delta}^{--}(1236)$ is compared with data at other energies and also with the crossed $pp \rightarrow \Delta^{++}n$ reaction. That the peaking of the momentum transfer tends to be greater for the $pp \rightarrow \Delta^{++}n$ than for the $\bar{p}n \rightarrow \bar{\Delta}^{--}p$ reaction at 5.5 GeV/c can be explained by using a simple Regge-pole model. For events produced without resonance in the final state, the longitudinal phase-space analysis is applied to the data. For these events, an attempt was also made to use a double Regge-pole model to describe the production. The present version of this model reproduces the experimental data fairly well. Using the Fermi motion of the neutron target, we try to extract information about the variation of the $\bar{p}n \rightarrow \bar{p}p\pi^-$ cross section with c.m. energy. In connection with this problem, a discussion on the validity domain of the impulse approximation is given.

I. INTRODUCTION

IN this paper, we investigate the $\bar{p}n \rightarrow \bar{p}p\pi^-$ reaction produced at 5.5 GeV/c. About 150 000 photographs were taken at the ZGS with the 30-in. deuterium-filled bubble chamber. The beam momentum was 5.55 GeV/c, with a spread of 0.054 GeV/c. Part of the film was scanned twice for events with at least one positive track stopping in the chamber. The data presented here are based on 7809 measured four-pronged events.

The experimental procedure and the selection of events assumed to be produced from $\bar{p}n$ interactions are discussed in Sec. II. Section III is devoted to the various fits made on the effective-mass distributions, while Sec. IV treats the production and decay of the $\bar{\Delta}^{--}(1236)$ resonance. In Sec. V we analyze the production of the $\bar{p}n \rightarrow \bar{p}p\pi^-$ reaction in a region of phase space where no resonances are produced. An attempt to obtain information about the variation of the $\bar{p}n \rightarrow \bar{p}p\pi^-$ cross section with energy is made in Sec. VI, together with an estimate of the cross section for the reaction under study.

II. EXPERIMENTAL PROCEDURE

The events were measured with conventional measuring machines connected on-line with an IBM 1800 computer, and processed through the CERN chain of programs. The $\bar{p}d \rightarrow p_s\bar{p}p\pi^-$ events were identified by kinematical fitting and comparison between the observed and calculated track ionizations. After cuts on the χ^2 and the missing-mass-squared distributions, we finally retained 986 events.

We show in Fig. 1 the momentum distributions of the two protons in the final state, the spectator being defined as the proton of lower fitted momentum. The shaded area corresponds to the faster proton. The momentum distribution of the spectator is corrected for scanning losses for p_s momenta bigger than 0.10 GeV/c. We obtain corrections of 16.2, 8.4, and 9.0% for the momentum bands 0.10–0.12, 0.12–0.14, and 0.14–0.16 GeV/c, respectively. No losses are observed beyond 0.16 GeV/c. For p_s momentum less than 0.1 GeV/c, the scanning losses are too important to allow any corrections. The full curve of Fig. 1, deduced from the Hulthén wave function, shows good agreement with the data even in the high-momentum region.

In Fig. 2 we present the laboratory angular distribution of the spectator for all the events and those having p_s momentum greater than 0.1 GeV/c (shaded area). The distribution represented by the shaded area is corrected for scanning losses. This correction was made by weighting each event having its p_s in the 0.10–0.16 GeV/c momentum range by a factor calculated from the losses estimated above. The distribution obtained with the total number of events agrees with isotropy. This agreement and those obtained in Fig. 1 between the full

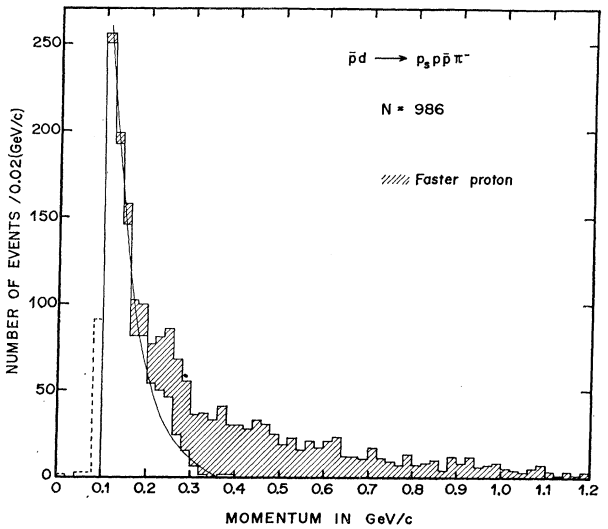

FIG. 1. Momentum distributions of the two protons in the laboratory system. The shaded area corresponds to the faster proton. The spectator distribution is corrected for scanning losses for p_s momentum greater than 0.1 GeV/c. The curve is deduced from the Hulthén wave function.

* Also from the Institut für Hochenergiephysik der Universität Heidelberg, Heidelberg, Germany.

line and the data are predicted by the simplified version of the impulse approximation. In this model one neglects flux-factor corrections, screening or shadow effects, and variation of the $\bar{p}d \to p_s\bar{p}p\pi^-$ cross section in the available c.m. energy range due to the Fermi motion of the target. The curve in Fig. 2, normalized to the shaded area, is obtained from the impulse approximation taking now into account flux-factor corrections and the cut made on the p_s momentum. That the agreement between this curve and the data is rather poor can be explained by assuming that the variation of the cross section (and perhaps also of the screening effects) with M, the $\bar{p}n$ c.m. energy, compensates the influence of the flux factor. Our reasoning is then the following: We consider that the impulse approximation is an acceptable description of the production as concerns the $\bar{p}n \to \bar{p}p\pi^-$ reaction. In particular, we admit that the $\bar{p}p\pi^-$ system results from a $\bar{p}n$ interaction. This is assumed to be true for all of the 986 events, because of the agreement between the experimental and calculated p_s momentum distributions (Fig. 1). However, for the attempt to extract from our data the variation of the $\bar{p}n \to \bar{p}p\pi^-$ cross section with M, a more careful examination of the validity domain of the impulse approximation will be made in Sec. VI.

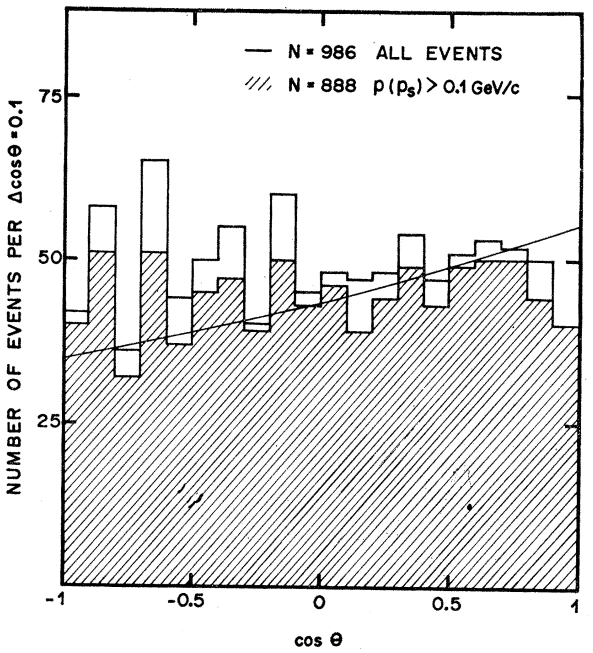

FIG. 2. Laboratory angular distribution of the spectator. The shaded area corresponds to events where the p_s momentum is greater than 0.1 GeV/c, corrected for scanning losses. The curve normalized to the shaded area is the prediction obtained from the impulse approximation taking the flux factor and the p_s momentum cut into account.

III. RESONANCE PRODUCTION

We show in Fig. 3 the $M_{\bar{p}\pi^-}$, $M_{p\pi^-}$, and $M_{\bar{p}p}$ effective-mass distributions. In this figure one observes a pronounced $\bar{\Delta}(1236)$ production and a bump in the vicinity of $M_{\bar{p}\pi^-} \sim 1.9$ GeV/c^2. The $M_{\bar{p}\pi^-}$ distribution was fitted by an incoherent mixture of two Breit-Wigner functions due to the $\bar{\Delta}(1236)$ and $\bar{\Delta}(1918)$ resonances and peripheral phase space [full line of Fig. 3(a)]. This phase space was obtained by the Monte Carlo method weighting each event by a factor $\exp(At_{\bar{p}\bar{p}}+Bt_{\bar{p}\bar{p}}^2)$, where $t_{\bar{p}\bar{p}}$ is the momentum transfer between the incoming and the outgoing $\bar{p}$. The A and B are constants fitted from the experimental $t_{\bar{p}\bar{p}}$ distribution. As can be seen in Fig. 3(a), the agreement between the data and the fitted curve is poor in the $M_{\bar{p}\pi^-} \sim 1.9$-GeV/$c^2$ region. The selection of events with $M_{p\pi^-} > 1.32$ GeV/c^2, i.e., outside the $\Delta^0(1236)$ region [dashed histogram of Fig. 3(a)], decreases the 1.9-GeV/c^2 bump although some weak enhancement remains. The dashed line, which is the fit to the $M_{\bar{p}\pi^-}$ mass spectrum with $M_{p\pi^-} > 1.32$ GeV/c^2 still using an incoherent mixture of peripheral phase space and two Breit-Wigner functions, agrees better with the data.

The $M_{p\pi^-}$ distribution does not show a clear structure in the vicinity of $M_{p\pi^-} \sim 1.236$ GeV/c^2. Examination of the Dalitz plot [Fig. 4(a)] shows that the events which contribute to the $\bar{p}\pi^-$ bump at 1.9 GeV/c are mainly concentered in the $\Delta^0(1236)$ band ($1.16 < M_{p\pi^-} < 1.32$ GeV/c^2). On the other hand, one sees also in the same band a depopulation of events in the region defined by

$$1.4 < M_{\bar{p}\pi^-} < 1.7 \text{ GeV}/c^2.$$

One may note that a similar depopulation of events was observed in the $pp \to pn\pi^+$ reaction at 7 GeV/c.[1] This lack of events is the reason for the fact that the $M_{p\pi^-}$ distribution is without clear structure in the $M_{p\pi^-} \sim 1.236$-GeV/c^2 region.

The full curves on Figs. 3(b) and 3(c), normalized to the total number of events, are obtained from a mixture of peripheral phase space and reflection due to $\bar{\Delta}^{--}(1236)$ production, the proportions being fixed from the fit to the $M_{\bar{p}\pi^-}$ mass spectrum. For calculating this reflection, we have also taken into account the strong peripherality of the $\bar{\Delta}^{--}(1236)$ production. These curves do not follow the experimental distributions. Even by selecting events outside the $\bar{\Delta}^{--}$ region, i.e., $M_{\bar{p}\pi^-} > 1.32$ GeV/c^2 [the dashed part of Figs. 3(b) and 3(c)], and using only peripheral phase space, modified according to the selection criterion $M_{\bar{p}\pi^-} > 1.32$ GeV/c^2, we do not have a better agreement [dashed lines of Figs. 3(b) and 3(c)]. The poor agreement of some of the effective-mass distributions was often observed in nucleon-nucleon or nonannihilation antinucleon-nucleon interactions. In fact, fits to effective-mass spectra are easily obtained when important bumps are present with small background, as is the case here for the $M_{\bar{p}\pi^-}$ distribution.

The peripheral phase space used does not reproduce the experimental peaking of the two baryons in the c.m.

[1] G. Alexander, Z. Carmel, Y. Eisenberg, E. E. Ronat, A. Shapira, G. Yekutieli, A. Fridman, G. Maurer, J. Oudet, G. Zech, and P. Cüer, Phys. Rev. **173**, 1322 (1968).

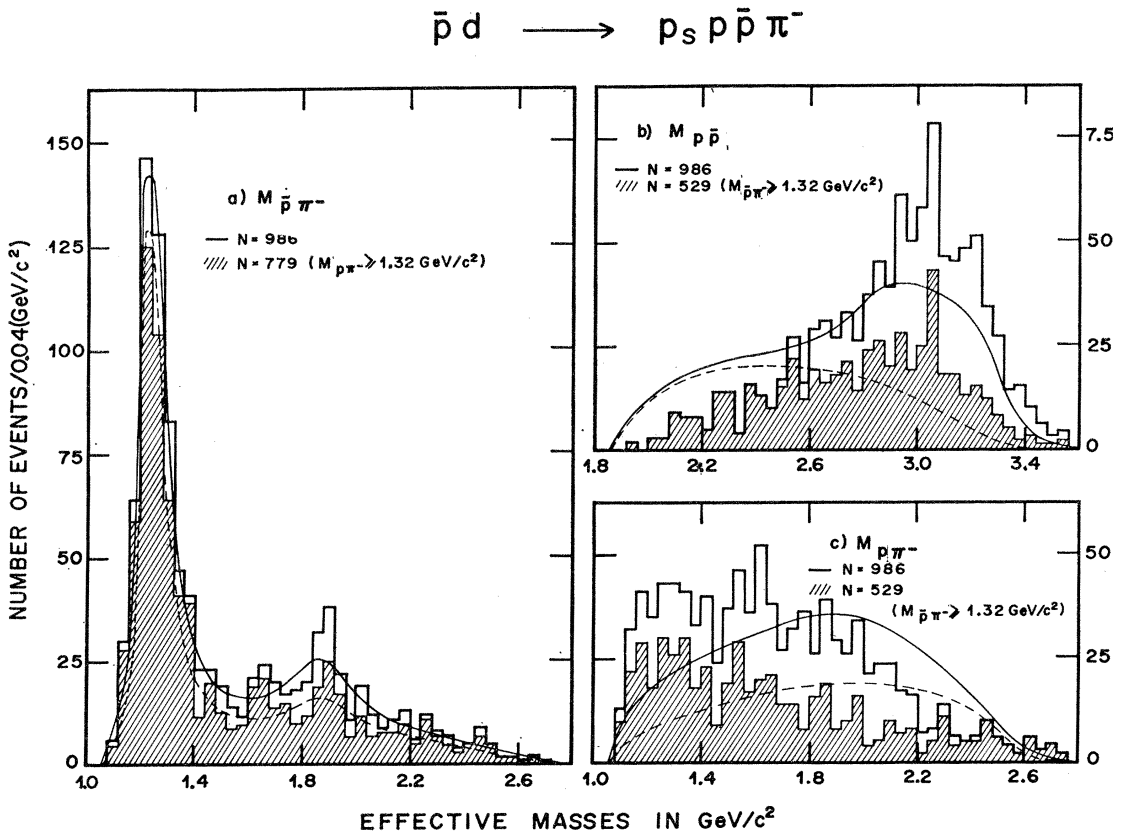

FIG. 3. Various effective-mass distributions. (a) The full and dashed lines represent, respectively, the fits to the $M_{\bar{p}\pi^-}$ mass spectra without and with the $M_{p\pi^-} \geq 1.32$ GeV/c^2 selection criterion. (b) and (c) The shaded area corresponds here to events with $M_{\bar{p}\pi^-} \geq 1.32$ GeV/c^2. The solid lines, normalized to the total number of events, are obtained from an incoherent mixture of peripheral phase space and reflection due to the $\bar{\Delta}(1236)$. The dashed curves represent peripheral phase space normalized to the shaded area.

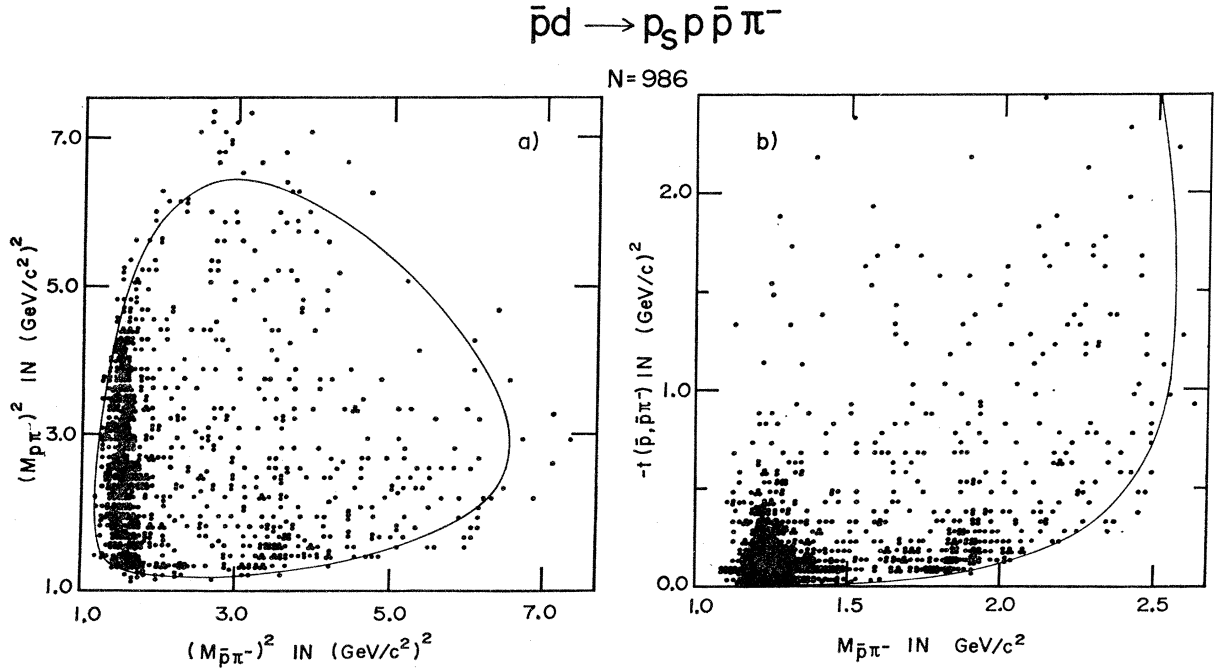

FIG. 4. Dalitz and Chew-Low plots for the $\bar{p}n \to \bar{p}p\pi^-$ reaction. The contours are calculated by assuming that the neutron target is at rest in the laboratory system. Here $t(\bar{p}, \bar{p}\pi^-)$ is the momentum transfer between the incident $\bar{p}$ and the outgoing $\bar{p}\pi^-$ systems.

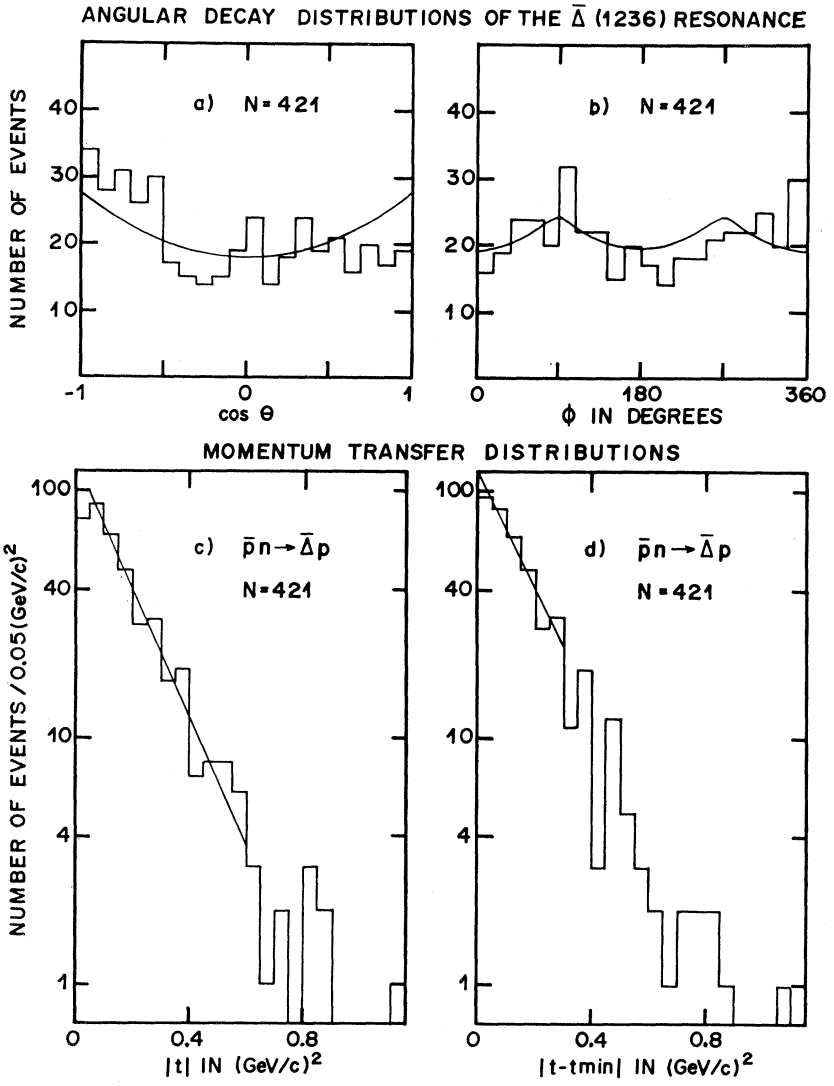

FIG. 5. (a) and (b) Decay angular distribution of the $\bar{\Delta}(1236)$ resonance. The curves are obtained from the ρ_{33} and $\mathrm{Re}\rho_{3-1}$ density-matrix elements. (c) and (d) The curves are obtained by fitting the data with $e^{b_1|t|}$ and $e^{b_2|t-t_{\min}|}$ functions.

system. Since this peaking deforms at most the $M_{\bar{p}p}$ distribution, we have also generated, with the Monte Carlo method, phase-space events according to the experimental $M_{\bar{p}p}$ distribution, weighting each event by an $\exp(At_{\bar{p}\bar{p}})$ factor. The use of this background does not improve the fit of the data. Therefore, we give only the percentage of $\bar{\Delta}^{--}$ production in the $\bar{p}n \to \bar{p}p\pi^-$ channel based on the fitted curve shown in Fig. 3(a) which is estimated to be $(51\pm4)\%$.

IV. PRODUCTION AND DECAY OF $\Delta^{--}(1236)$ RESONANCE

The $\bar{\Delta}^{--}$ is emitted along the beam direction as can be seen from the Chew-Low plot [Fig. 4(b)] and the $|t|$ or $t'=|t-t_{\min}|$ distributions (Fig. 5). Here t is the four-momentum transfer between the incident $\bar{p}$ and the produced $\bar{\Delta}^{--}$, while $|t_{\min}|$ is the smallest possible $|t|$ for each $M_{\bar{p}\pi^-}$ value. The $\bar{\Delta}$ resonance is defined by $1.16<M_{\bar{p}\pi^-}<1.32$ GeV/c.

For the entire t range, we have evaluated the density-matrix elements:

$$\rho_{33}=0.17_{-0.02}{}^{+0.03},$$
$$\mathrm{Re}\rho_{3-1}=0.04\pm0.02,$$
$$\mathrm{Re}\rho_{31}=0.04\pm0.03.$$

In Figs. 5(a) and 5(b) we show the decay angular distributions of the $\bar{\Delta}^{--}$ in the Jackson reference frame.[2] The curves are calculated from the ρ_{33} and $\mathrm{Re}\rho_{3-1}$

TABLE I. Slopes obtained by fitting the momentum transfer distributions of the $\bar{p}n \to \bar{\Delta}^{--}p$ reaction at 5.5 GeV/c.

$\lvert t\rvert$ range used $(\mathrm{GeV}/c)^2$	b_1 $(\mathrm{GeV}/c)^{-2}$	t' range used $(\mathrm{GeV}/c)^2$	b_2 $(\mathrm{GeV}/c)^{-2}$
0.05–0.40	6.0±0.2	0.0–0.3	5.2±0.3
0.05–0.60	6.0±0.2	0.0–0.4	5.9±0.2

[2] J. D. Jackson, Nuovo Cimento **34**, 1644 (1964).

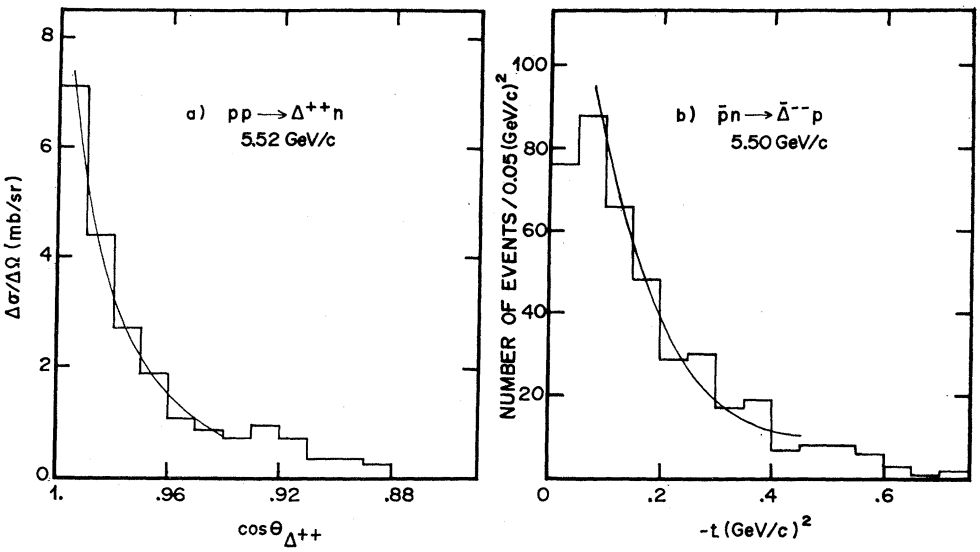

FIG. 6. Production of Δ^{++} and $\bar{\Delta}^{--}$ resonances in pp and $\bar{p}n$ interactions at ~5.5 GeV/c. (a) Folded angular distribution of the Δ^{++} in the c.m. system for the $pp \to \Delta^{++}n$ reaction taken from Ref. 4. (b) Momentum transfer distribution for the $\bar{p}n \to \bar{\Delta}^{--}p$ reaction. The curves represent the fits obtained with a simplified Regge-pole model (see text).

density-matrix elements. The forward-backward asymmetry observed in Fig. 5(a) shows the influence of the background events in the $1.16 < M_{\bar{p}\pi^-} < 1.32$-GeV/$c^2$ range.

The curves of Figs. 5(c) and 5(d) are fitted with $e^{b_1|t|}$ and $e^{b_2 t'}$ functions. Table I gives the fitted values for different $|t|$ and t' ranges. As can be seen from this table, the slope b_1 is not sensitive to the $|t|$ range used for the data fitting.

In Table II, we compare the slopes obtained at different energies for the $\bar{p}n \to \bar{\Delta}^{--}p$ and $pp \to \Delta^{++}n$ reactions. As already pointed out in Ref. 3, the peaking of the t distribution for the $\bar{p}n \to \bar{\Delta}^{--}p$ reaction seems to decrease with increasing incident momentum. One notes also in this table that the slope b_1 is greater for $pp \to \Delta^{++}n$ than for the $\bar{p}n \to \bar{\Delta}^{--}p$ reaction.

TABLE II. Comparison of the slopes b_1 obtained at different energies for the $\bar{p}n \to \bar{\Delta}^{--}p$ and $pp \to \Delta^{++}n$ reactions. Apart from the present data and those from Ref. c the b_1 were obtained by fitting the published histograms.

Incident momentum (GeV/c)	Ref.	Reaction	$\|t\|$ range used (GeV/c)^2	b_1 (GeV/c)$^{-2}$
1.96	a	$\bar{p}n \to \bar{\Delta}^{--}p$	0.04–0.40	8.3±0.4
5.5	b		0.05–0.40	6.0±0.2
7.0	c		0.0 –0.50	5.6±0.7
5.52	d	$pp \to \Delta^{++}n$	0.03–0.24	11.2±0.4
7.0	e		0.06–0.17	15.8±2.9

[a] T. C. Bacon *et al.*, Phys. Rev. 139, B1420 (1965).
[b] This experiment.
[c] Johns Hopkins University Group (private communication), based on preliminary results.
[d] Reference 4.
[e] Reference 1.

For these two reactions, the same particles or Regge trajectories will be exchanged with equal strengths in the t channel. Therefore, on the basis of an absorption model with one-particle exchange, only an important difference in the absorption will reproduce the actual t dependence at 5.5 GeV/c. We have then preferred to fit the t distributions of both $\bar{p}n \to \Delta^{--}p$ and $pp \to \Delta^{++}n$ reactions at ~5.5 GeV/c with a Regge-pole model, using the following simplified form for the amplitude:

$$A^s = \sum_i \beta_i(t)\xi_i(t)[2\alpha_i(t)+1]\left(\frac{s-u}{2s_0}\right)^{\alpha_i(t)} \equiv \sum_i \beta_i(t)T_i(t).$$

The α_i are the trajectories exchanged in the t channel, $\xi_i(t)$ and $\beta_i(t)$ being, respectively, their signatures and residue functions, while the scaling factor s_0 is taken as 1 GeV^2.

The $\bar{p}n \to \bar{\Delta}^{--}p$ reaction is related to the $pp \to \Delta^{++}n$ reaction by crossing from s to u channels. According to Regge-pole theory, the u-channel amplitude is obtained from the s-channel amplitude by changing the signs of the contributions due to trajectories of odd signature. The use of ρ and A_2 trajectories cannot reproduce the t dependence of both reactions at the same energy if these trajectories are assumed to be degenerate. Even the "weak" form of exchange degeneracy $[\beta_\rho(t) \neq \beta_{A_2}(t)]$ gives equal slopes for the momentum transfer distributions.

Therefore, we consider the exchange of the π, ρ, and A_2 trajectories given by

$$\alpha_\pi = -0.022 + 1.1t, \quad \alpha_\rho = \alpha_{A_2} = 0.57 + t,$$

[3] H. Braun, D. Evrard, A. Fridman, J.-P. Gerber, E. Lesquoy, G. Maurer, A. Michalon, B. Schiby, R. Strub, C. Voltolini, and P. Cüer, report presented at the APS Meeting, Boulder, Colorado, 1969 (unpublished).

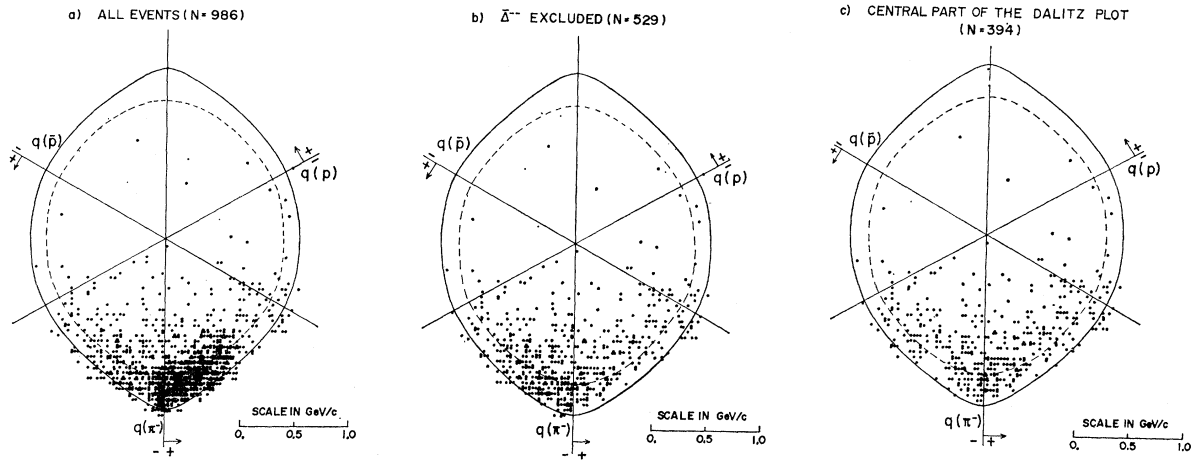

FIG. 7. Van Hove plots for the $\bar{p}n \to \bar{p}p\pi^-$ reactions. The contours are calculated assuming that the neutron target is at rest in the laboratory system, and that the secondaries have vanishing transverse momenta. The dashed curves are obtained with the following set of transverse momenta: $r_1=0.39$ GeV/c, $r_2=0.41$ GeV/c, and $r_3=0.44$ GeV/c. These values correspond to the mean $p_\perp$ of the p, $\bar{p}$, and π^-, respectively.

with t in $(\mathrm{GeV}/c)^2$, assuming an $e^{B_i t}$ dependence for the residue functions.

We show in Fig. 6 the Δ^{++} angular c.m. distribution for the $pp \to \Delta^{++}n$ reaction, taken from Ref. 4, and the momentum transfer distribution for the $\bar{p}n \to \bar{\Delta}^{--}p$. An over-all fit was made on these two histograms using the following expression:

$$A^s = K\{e^{B_1 t} T_\pi(t) + [a_A T_A(t) \pm a_\rho T_\rho(t)] e^{B_2 t}\}$$

in the t intervals of

$$0.004 < |t| < 0.246 \ (\mathrm{GeV}/c)^2 \text{ for reaction } pp \to \Delta^{++}n$$

and

$$0.05 < |t| < 0.45 \ (\mathrm{GeV}/c)^2 \text{ for reaction } \bar{p}n \to \bar{\Delta}^{--}p.$$

Here K is a normalization factor. The positive (negative) sign in A^s corresponds to the $pp \to \Delta^{++}n$ ($\bar{p}n \to \bar{\Delta}^{--}p$) reaction.

The fit shows that B_1 is compatible with zero. Taking $B_1=0$, we obtain the following values of the parameters:

$$a_A = 1.88 \pm 0.25, \quad a_\rho = 0.714 \pm 0.266,$$
$$B_2 = 3.2 \pm 0.3 \ (\mathrm{GeV}/c)^{-2}$$

(confidence level of 35%).

As can be seen in Fig. 6, there is good agreement between the fitted curves and the experimental data. However, the use of such a simplified matrix element would be really justified if similar fits could be made at other c.m. energies.

V. FINAL STATE WITHOUT RESONANCES

In the following, we attempt to analyze the production of events located in central part of the Dalitz plot [Fig. 4(a)], i.e., in the region where practically no resonance production is observed.

This region is defined by

$$M_{\bar{p}\pi^-} = S_{\bar{p}\pi^-}^{1/2} > 1.32 \ \mathrm{GeV}/c^2,$$
$$M_{p\pi^-} = S_{p\pi^-}^{1/2} > 1.32 \ \mathrm{GeV}/c^2.$$

For high-energy production the transverse momenta of the outgoing particles generally have similar distributions and small mean values. This also is the case here (see also Fig. 13) where the mean transverse momenta of the p, $\bar{p}$, and π^- are, respectively,

$$\langle p_\perp(p) \rangle = r_1 = 0.39 \ \mathrm{GeV}/c,$$
$$\langle p_\perp(\bar{p}) \rangle = r_2 = 0.41 \ \mathrm{GeV}/c,$$
$$\langle p_\perp(\pi^-) \rangle = r_3 = 0.44 \ \mathrm{GeV}/c.$$

Information about specific production mechanism may be obtained more easily by studying the c.m. longitudinal momentum distributions of the secondaries. We have then presented our data in the form suggested in Ref. 5, i.e., using the Van Hove or longitudinal phase-space plot. Figures 7(a)–7(c) show, respectively, such plots for all the 986 events, for the sample obtained by excluding the $\bar{\Delta}^{--}p$ final state, and finally for the events located in the central part of the Dalitz plot. The $q(m)$ in Fig. 7 is the longitudinal momentum of particle m in the $(\bar{p}n)$ c.m. system. The full lines represent the kinematical boundaries obtained with vanishing transverse momenta of the outgoing particles, while the dashed lines were obtained with transverse momenta equal to $\langle p_\perp(p) \rangle$, $\langle p_\perp(\bar{p}) \rangle$, and $\langle p_\perp(\pi^-) \rangle$.

The increase of the density of points in Figs. 7(a) and 7(b) corresponds to the influence of the $\bar{\Delta}^{--}$ and Δ^0 production. Indeed, because of the strong peripherality of the reaction, the decay products of the resonances tend to be emitted in the same hemisphere in the c.m.

[4] G. Alexander, O. Benary, O. Czapek, B. Haber, N. Kidron, B. Reuter, A. Shapira, E. Simopoulou, and G. Yekutieli, Phys. Rev. **154**, B1284 (1967).

[5] L. Van Hove, Nucl. Phys. **B9**, 331 (1969).

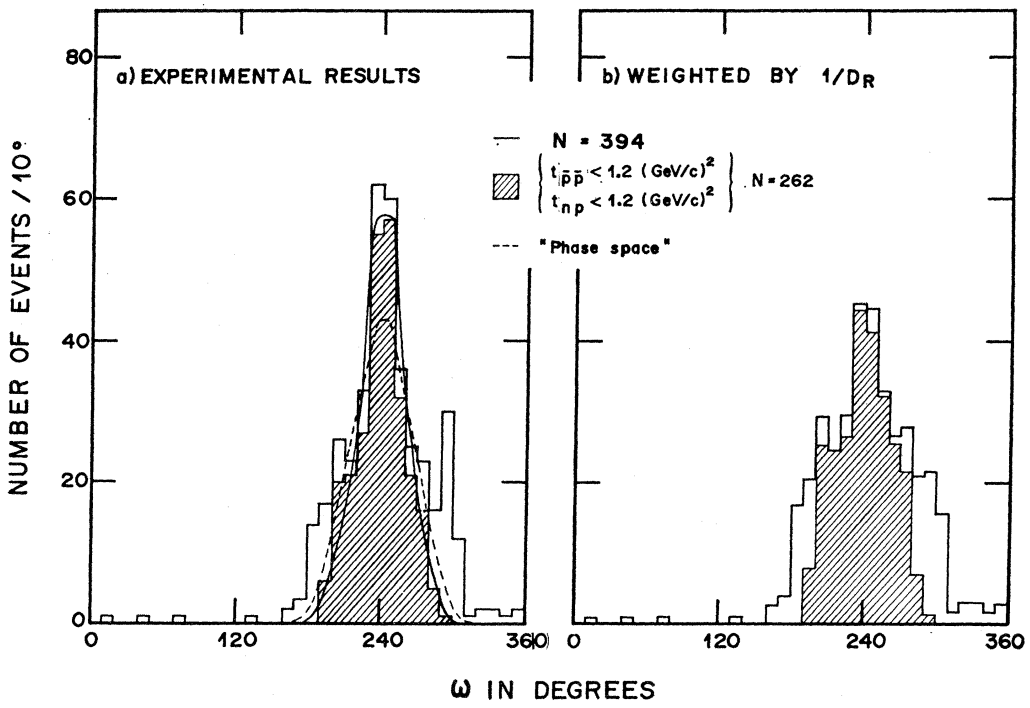

FIG. 8. Weighted and unweighted distribution of ω along the hexagon for events with $M_{p\pi^-}$ and $M_{\bar{p}\pi^-} > 1.32$ GeV/c^2. The shaded area corresponds to events with the additional $t_{\bar{p}\bar{p}}$, $t_{np} > -1.2$ (GeV/c)^2 cuts. The full and dashed lines, normalized to the shaded area, are, respectively, the predictions obtained with the chosen matrix element (see text) and with phase space modified according to our selection criteria.

system. This corresponds then to an increase of the point densities in the region of $q(\pi^-)$, $q(\bar{p})>0$ [Fig. 7(a)], and $q(p)$, $q(\pi^-)<0$ [Fig. 7(b)]. Figure 7(c) shows that the events fulfilling the $S_{\bar{p}\pi^-}{}^{-1/2}$, $S_{p\pi^-}{}^{-1/2} > 1.32$ GeV/c^2 conditions are concentrated in the angular interval of $180° < \omega < 310°$. Here ω is the angle along the hexagon as defined in Ref. 6 which increases counterclockwise from the line $q(p)=0$. In the limit of $p_\perp(\bar{p}) = p_\perp(p) = p_\perp(\pi^-) = 0$, this angle determines completely the longitudinal momentum configuration of the outgoing particles. From Fig. 7, one also sees that the events tend to be concentrated merely near the boundaries of the plots, which is due to the relative smallness of $p_\perp$ for $\bar{p}$, p, and π^-. In Fig. 8 we present the unweighted and weighted distributions of ω along the hexagon for the events under study, i.e., located in the central part of the Dalitz plot. The weighted distribution is obtained by weighting each event by $1/D_R$, the inverse of the Lorentz-invariant density factor.[5] For three particles in the final state, D_R is given by

$$D_R = \sum_{i=1}^{3} q(i)^2 \Big/ \left\{ \prod_{i=1}^{3} E(i) \frac{\sum q(i)^2}{E(i)} \right\},$$

where $E(i)$ is the energy of particle i in the c.m. system. Thus Fig. 8 gives information about the ω dependence of the matrix element squared describing the $\bar{p}n \to \bar{p}p\pi^-$ process, and shows also that the events tend to be distributed symmetrically around $\omega = 240°$ [line of $q(\pi)=0$]. This means that π^- is emitted with a rather small longitudinal momentum while the $\bar{p}$ (p) tend to be

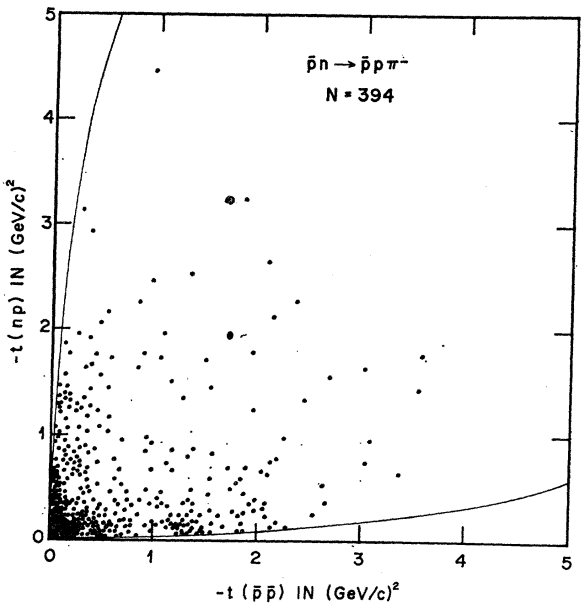

FIG. 9. Scatter plot of $t_2 = t(np)$ versus $t_1 = t(\bar{p}\bar{p})$. The kinematical contours are calculated by assuming that the neutron target is at rest in the laboratory system.

[6] F. Bigata, thesis, Paris University, 1968 (unpublished).

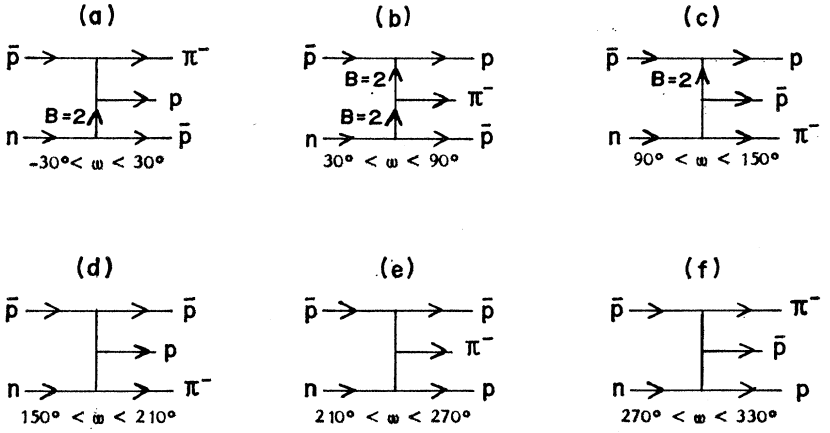

FIG. 10. The double-exchange graphs which can contribute to the $\bar{p}n \to \bar{p}p\pi$ reaction.

emitted in the forward (backward) hemisphere in the c.m. system.

Moreover, the $|t_{\bar{p}p}|$, $|t_{np}|$ scatter plot (Fig. 9) shows a concentration of events for small values of $|t_{np}|$ and $|t_{\bar{p}\bar{p}}|$, $t_{np}=t_2$ ($t_{\bar{p}\bar{p}}=t_1$) being the four-momentum transfer between the incident n ($\bar{p}$) and the outgoing p ($\bar{p}$). All this suggests a description of the production in terms of a double-Regge-pole model with dominant diagrams having the π^- emitted at the central vertex.

The double-exchange graphs which can contribute to the $\bar{p}n \to \bar{p}p\pi$ reaction are represented in Fig. 10. For these kinds of graphs, one generally admits that the final particles are in decreasing order of longitudinal momentum by going here from the top to the bottom of each diagram. Each graph corresponds then to given limits of the angle ω in the Van Hove plot. A tentative assignment of each event to one of the graphs can be made by classifying our data in six groups according to the decreasing order of $q(m)$ (see Table III). From Table III one sees that very few events can be attributed to the diagrams (a)–(c) which need an exchange of systems having baryonic number $B=2$. On the other hand, the number of events in groups (d) and (f) are relatively important. Some of these events are produced with $\bar{p}p$ pairs emitted in the same c.m. hemisphere. The cuts on the momentum transfers $|t_{\bar{p}\bar{p}}|$, $|t_{np}|<1.2$ (GeV/c)^2 suppress events in groups (a)–(c) and increase the ratio of events in group (e) to the sum of events in (d) and (f) (see Table III). The study of the remaining events in (d) and (f) shows now that the $\bar{p}$ (p) is always emitted forward (backward) in the c.m. system despite the fact that $q(\pi^-)<q(p)$ or $q(\pi^-)>q(\bar{p})$. We chose then to consider all the 262 events obtained after the $t_{\bar{p}\bar{p}}$ and t_{np} cuts as being due mainly to graphs with the π^- emitted at the central vertex.

TABLE III. Number of events located in the central part of the Dalitz plot, classified into six groups according to decreasing order of q.

Graphs and $q(m)$ order	(a) $\pi^-, p, \bar{p}$	(b) $p, \pi^-, \bar{p}$	(c) $p, \bar{p}, \pi^-$	(d) $\bar{p}, p, \pi^-$	(e) $\bar{p}, \pi^-, p$	(f) $\pi^-, \bar{p}, p$
No t_1, t_2 cuts	6	2	1	62	239	84
$t_1, t_2 > -1.2$ (GeV/c)^2	...	...	...	26	214	22

For these events, the $t_{\bar{p}\bar{p}}$ and t_{np} distributions (shaded areas of Fig. 11) are very similar. Although the $\bar{\Delta}^{--}$ tail still has a small influence on the $M_{\bar{p}\pi^-}$ distribution, one also sees from this figure that the $M_{p\pi^-}$ and $M_{\bar{p}\pi^-}$ mass spectra show some similarity. A possible way to reproduce these features is to use diagrams (a) and (b) of Fig. 12 in order to explain the production of these 262 events. Assuming that these graphs can be added incoherently, we use the following approximation for the spin-averaged invariant matrix element squared:

$$|T|^2 = N_0 V,$$

with

$$V = \left(\frac{S_{\bar{p}\pi}}{S_1}\right)^{2\alpha_\pi(t_1)} \left(\frac{S_{p\pi}}{S_2}\right)^{2\alpha_\rho(t_2)} + \left(\frac{S_{p\pi}}{S_3}\right)^{2\alpha_\pi(t_2)} \left(\frac{S_{\bar{p}\pi}}{S_4}\right)^{2\alpha_\rho(t_1)},$$

N_0 being a normalization factor.

A maximum-likelihood fit to the data in the four-dimensional space formed by the variables $S_{\bar{p}\pi^-}$, $S_{p\pi^-}$, t_1, and t_2 permits us to adjust the values of the S_1, S_2, S_3, and S_4 factors.

In order to reproduce the general features just mentioned above (similar distributions of $t_{\bar{p}\bar{p}}$, t_{np} and $M_{\bar{p}\pi^-}$, $M_{p\pi^-}$), one must have

$$S_1 \sim S_3, \quad S_2 \sim S_4.$$

By fitting the data, we have first verified that this indeed is the case; then imposing the $S_1=S_3$ and $S_2=S_4$ conditions, we obtain the following fitted values:

$$S_1 = 0.29 \pm 0.09 \text{ GeV}^2, \quad S_2 = 1.21 \pm 0.21 \text{ GeV}^2.$$

The curves shown in Fig. 11 (t_{np}, $t_{\bar{p}\bar{p}}$, $M_{\bar{p}\pi^-}$, and $M_{p\pi^-}$ distributions) are the results obtained from this fit. In

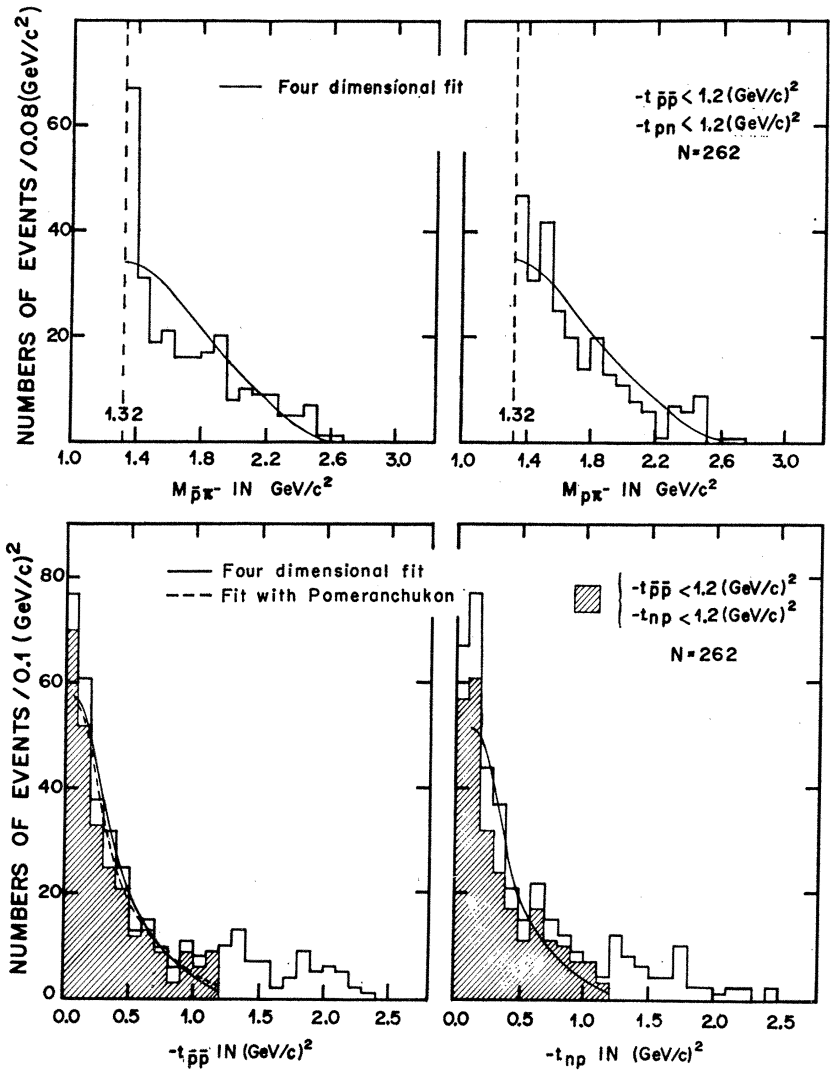

FIG. 11. Effective-mass and momentum-transfer distributions for events with $M_{\bar{p}\pi^-}$ and $M_{p\pi^-}>1.32$ GeV/c^2. The full lines represent the maximum-likelihood fits to the data selected according to $M_{\bar{p}\pi^-}$, $M_{p\pi^-}>1.32$ GeV/c^2, and $t_{p\bar{p}}$, $t_{np}>-1.2$ (GeV/c)^2 conditions, using a matrix element without Pomeranchukon exchange (see text). The nonshaded part of the $t_{\bar{p}\bar{p}}$ and t_{np} distributions are obtained for events with $M_{\bar{p}\pi^-}$, $M_{p\pi^-}>1.32$ GeV/c^2, but without $t_{\bar{p}p}$ and t_{np} cuts. The dashed line in the $t_{\bar{p}\bar{p}}$ distribution is the fitted curve obtained by including a graph with Pomeranchukon exchange.

Fig. 13 we present the longitudinal and transverse momentum distributions of the p, $\bar{p}$, and π^-. The dashed lines have been obtained from phase-space calculations deformed according to our selection criteria. The behaviors of the full curves calculated with the model described above are in satisfactory agreement with the experimental data.

We have also considered the possibility of a Pomeranchukon exchange at the $\bar{p}\bar{p}$ vertex [diagram (c) of Fig. 12]. The use of

$$|T|^2=N_0[V+AS_{\bar{p}\pi^-}{}^{-2}(S_{p\pi}/S_3)^{2\alpha_\pi(t)}]$$

for the maximum-likelihood fit to our data yields the

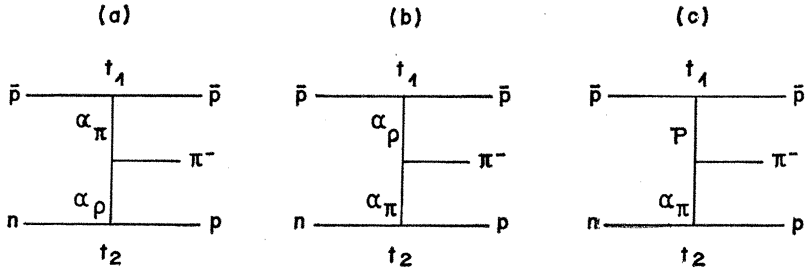

FIG. 12. Graphs which may contribute to the $\bar{p}n\to\bar{p}p\pi^-$ process.

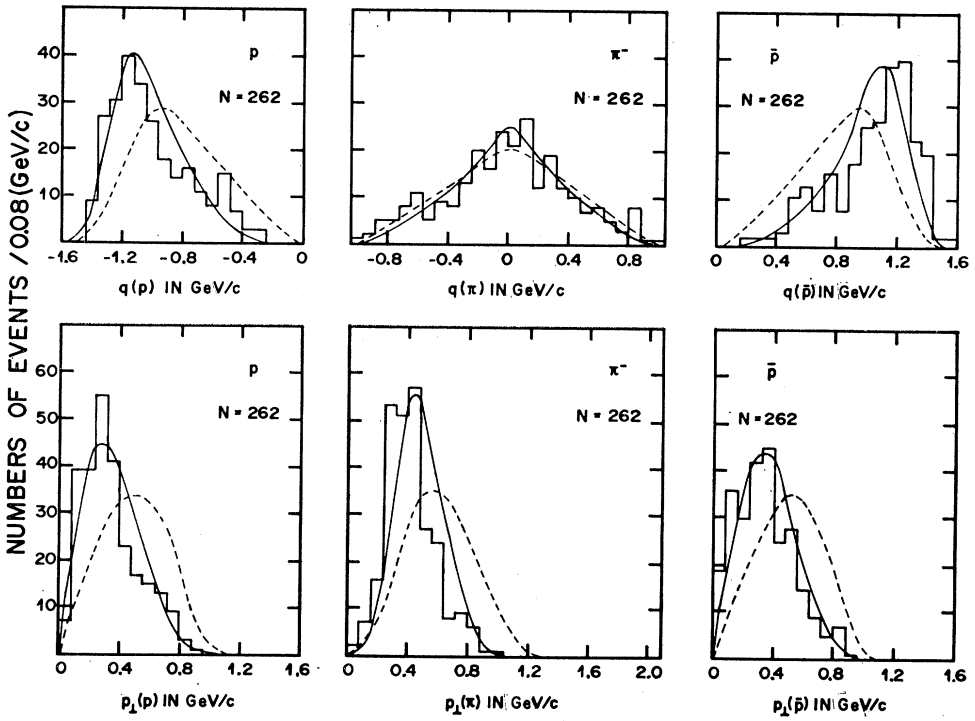

FIG. 13. Lonigtudinal and transverse momentum distribution of the secondaries for the events fullfilling the $M_{\bar{p}\pi^-}$, $M_{\bar{p}\pi^-} > 1.32$ GeV/c^2 and the $t_{\bar{p}\bar{p}}$, $t_{np} > -1.2$ (GeV/c)^2 conditions. The full lines are the predictions obtained from the double Regge model as described in the text. The dashed curves normalized to the total number of events are the phase-space predictions modified according to our selection criteria.

following values:

$$S_1 = 0.19 \pm 0.07 \text{ GeV}^2,$$
$$S_2 = 1.15 \pm 0.18 \text{ GeV}^2,$$
$$S_3 = 1.95 \pm 0.12 \text{ GeV}^2,$$
$$A = (0.17_{-0.05}^{+0.10}) \times 10^{-2}.$$

The constant A indicates the relative magnitude of the contribution of diagram (c) (Fig. 12) to the production. Because of the small A value, the calculated longitudinal and transverse momentum distributions with this new $|T|^2$ are practically identical to those obtained without diagram (c). However, somewhat better agreement with the shape of the experimental $t_{\bar{p}\bar{p}}$ distribution is obtained by including Pomeranchukon exchange (see Fig. 11).

In conclusion, we see that despite the crudeness of this approach, the model reproduces fairly well the experimental distributions, without a real need of Pomeranchukon exchange. By imposing $S_1 = S_3$, $S_2 = S_4$, the calculation has also shown that no appreciable difference appears in the calculated distributions if we take a coherent sum instead of an incoherent mixture of the two graphs (a) and (b) of Fig. 12.

VI. CROSS SECTION AND ITS VARIATION WITH c.m. ENERGY

A. Variation of Cross Section with c.m. Energy

The search for boson resonances of high masses coupled to the $(\bar{p}n)$ system can be made by studying $\bar{p}n$ formation experiments. Benefiting here from the internal motion of the neutron in the deuteron, we will attempt to obtain information about the variation of the $\bar{p}n \to \bar{p}p\pi^-$ cross section as a function of M, the $\bar{p}n$ c.m. energy.

For given beam and target velocities, the number N of events observed in a definite channel is related to the cross section σ by

$$N = \sigma \rho_1 \rho_2 F V T, \tag{1}$$

where, as usual, ρ_1 and ρ_2 are, respectively, the density of the beam and the target particles in their own rest frames. F is the Møller factor and VT defines the four-dimensional observation volume.

In the case of a neutron target moving in the deuteron, the equivalent of formula (1) can be written as

$$\frac{d^2N}{dp_s\, d\cos\theta_s} = \sigma' \rho_1 \rho_2 F V T |\Phi(p_s, \cos\theta_s)|^2, \tag{2}$$

where p_s, $\cos\theta_s$, and $\Phi(p_s, \cos\theta_s)$, the ground-state wave function of the deuteron, are expressed here in the laboratory system. For convenience, instead of considering the neutron target, p_s and θ_s were chosen as being the momentum of the spectator proton and the angle between the spectator and the incident $\bar{p}$.[7]

[7] Throughout this section, p_s will denote the momentum of the spectator.

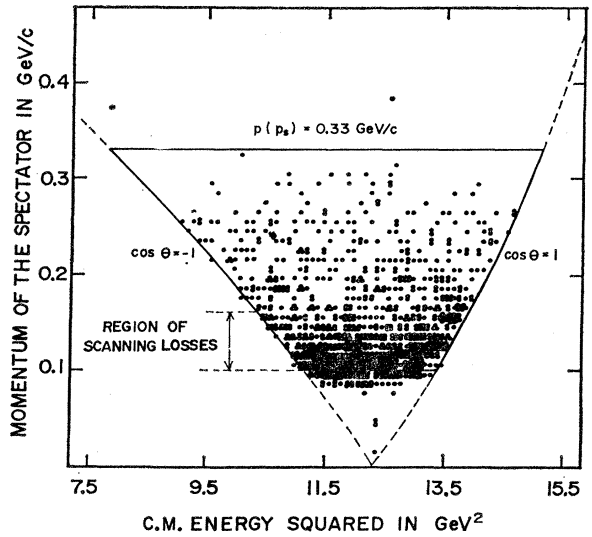

FIG. 14. Scatter plot of p_s versus M^2. This plot shows the distribution of events in the allowed kinematical region given by two hyperbola branches which correspond, respectively, to $\cos\theta = -1, +1$. Here θ is the angle between the spectator and the incident $\bar{p}$ in the laboratory system. Only events for which p (p_s), the momentum of the spectator, is $0.10 \leq p$ $(p_s) \leq 0.33$ GeV/c are taken for the present analysis (see text).

The formula (2), which implicitly assumes that the collision occurs with one of the bound nucleons, expresses quantitatively the first-order impulse approximation. The usual approximation consists in assuming that σ' is constant in the available c.m. energy range. Because of screening and off-mass-shell effects, σ' is, of course, not the free $\bar{p}n$ cross section. In order to obtain some information on the variation of the $\bar{p}n \to \bar{p}p\pi^-$ cross section with M, we attempt to extract σ' from our data when the screening or shadow effects are not too important. If, in addition, we neglect off-mass-shell effects, σ' in particular will depend on M only. We will then check if our data obey Eq. (2), with $\sigma' = \sigma'(M)$. This will be made in the manner described below.

Neglecting the D part of the deuteron wave function, one has

$$d(\cos\theta_s) = (1/2p_i p_s)dM^2;$$

hence

$$\frac{d^2N}{dp_s dM^2} = \frac{1}{2p_i p_s}\sigma'\rho_1\rho_2 FVT|\Phi(p_s)|^2 = A\sigma'\frac{F}{p_s}|\Phi(p_s)|^2, \quad (3)$$

p_i being the incident momentum. This is essentially the experimental $d^2N/dp_s dM^2$ distribution of our events in the (p_s, M^2) scatter plot shown in Fig. 14 which will be used throughout the following discussion. The points in Fig. 14 are in a region delimited by two hyperbola branches. For the present discussion, we will only consider events for which $0.1 < p_s < 0.33$ GeV/c (full lines of Fig. 14). The $p_s = 0.1$-GeV/c limit was chosen because for $p_s < 0.1$ GeV/c, the scanning losses are too large to allow any correction. For events with $0.1 < p_s < 0.16$ GeV/c, all of the experimental distributions considered will be weighted in order to take into account the scanning losses estimated in Sec. II.

Since the Møller factor is a function of both variables p_s and M^2, let us consider the $dN'/dM^2 dp_s$ distribution for which each event is weighted by p_s/F. Then

$$\frac{d^2N'}{dp_s dM^2} = A|\Phi(p_s)|^2\sigma'$$

is a product of two functions depending, respectively, on p_s and M^2, if $\sigma' = \sigma'(M)$.

The dN'/dp_s distribution in a certain region of $M_1^2 < M^2 < M_2^2$ is then given by

$$\frac{dN'}{dp_s} = A|\Phi(p_s)|^2\int_{M_1^2(p_s)}^{M_2^2(p_s)}\sigma'(M)dM^2.$$

In order to avoid the p_s dependence of the $M_1^2(p_s)$ and $M_2^2(p_s)$ limits, one can evaluate dN'/dp_s in a rectangle[6] of an allowed region of the (p_s, M^2) scatter plot $(M_1^2 < M^2 < M_2^2,\ p_1 < p_s < p_2)$; hence

$$dN'/dp_s = |\Phi(p_s)|^2 K.$$

K is a quantity depending on the unknown function σ', assumed to depend on M only, but the M_1^2 and M_2^2 limits are independent of p_s, the momentum of the spectator.

In such a rectangle, one can test whether the impulse approximation holds and whether $\sigma' = \sigma(M)$ by comparing the experimental dN'/dp_s distribution with $K|\Phi(p_s)|^2$. In order to eliminate K in the comparison procedure, let us define for each event the normalized function

$$P(p_s) = \int_{p_1}^{p_s}\frac{dN'}{dp_s}dp_s \Big/ \int_{p_1}^{p_2}\frac{dN'}{dp_s}dp_s = \int_{p_1}^{p_s}|\Phi(p_s)|^2 dp_s \Big/ \int_{p_1}^{p_2}|\Phi(p_s)|^2 dp_s.$$

The dN'/dP distribution (for which each event is weighted by p_s/F in addition to the extra weight due to

TABLE IV. Values of χ^2/n for different bands of the $(\bar{p}n)$ c.m. energy. The χ^2 and χ'^2 values are obtained by fitting in each M bin the dN'/dP distributions to a straight line using, respectively, the Hulthén and the modified deuteron wave function; n is the number of degrees of freedom.

ΔM in GeV/c	Number of events	χ^2/n	χ'^2/n
3.26–3.32	60	1.5	1.4
3.32–3.38	106	4.1	4.1
3.38–3.44	107	5.8	1.9
3.44–3.50	119	0.1	0.3
3.50–3.56	113	1.1	1.4
3.56–3.62	121	0.9	0.3
3.62–3.68	106	9.7	7.4
3.68–3.74	57	1.8	2.1

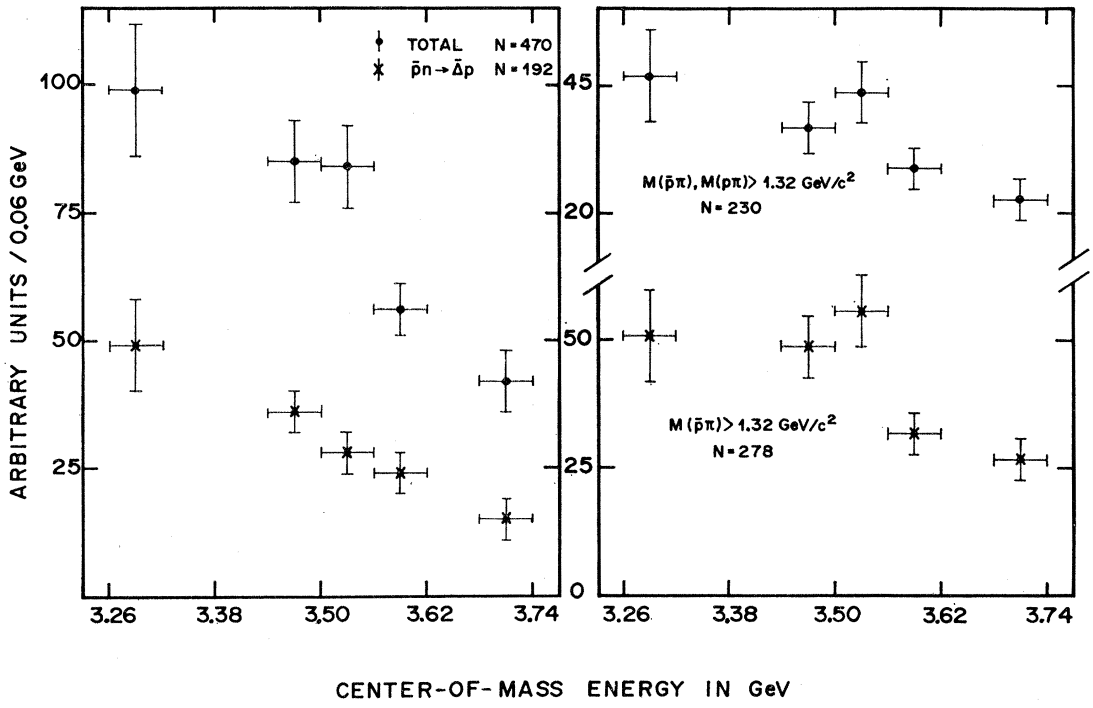

FIG. 15. Variation of σ' with the $(\bar{p}n)$ c.m. energy. The events contributing to this figure are chosen as described in the text.

the scanning losses) should have an isotropic distribution if the assumptions made above are correct. Such a test can be made for any elementary rectangle. Moreover, since we use a normalized $P(p_s)$ function, all the events in a given $M_1^2 < M^2 < M_2^2$ region can be taken for studying the dN'/dP distribution. In this case, $p_1 = p_{\min}(M)$, the minimum allowed p_s value for a given M, is calculated for each event individually, while p_2 is taken here as being 0.33 GeV/c. (We have checked that the conclusions drawn below are not sensitive to the particular p_2 value chosen.)

For $M < 3.26$ GeV/c^2 or $M > 3.74$ GeV/c^2, one observes a very important asymmetry in the dN'/dP distributions; we have therefore divided the range of $3.26 < M < 3.74$ GeV/c^2 into bins of $\Delta M = 60$ MeV for which we have studied the dN'/dP distributions. Table IV indicates, for each bin, the number of events used and the χ^2/n value obtained by fitting the dN'/dP to a straight line, n being the number of degrees of freedom.

We took for the Hulthén wave function

$$\Phi(p_s) = p_s/(p_s^2+\alpha^2)(p_s^2+\beta^2),$$

with $\alpha = 0.0456$ (GeV/c)^2 and $\beta = 0.260$ (GeV/c)^2.

For calculating σ' we use only bins with $\chi^2/n < 1.8$, which corresponds here to a confidence level greater than 13%.

For these events, we estimate $\sigma'(M)$ by means of the formula

$$\sigma'(M) \simeq \Delta N'/\Delta M,$$

each event in the ΔM bin being weighted individually by

$$W_i = \frac{1}{MF/p_s|\Phi(p_s)|^2} \quad \text{[see Eq. (3)]}$$

in addition to an extra weight due to scanning losses. Figure 15 represents σ' in arbitrary units as a function of M for the $\bar{p}n \to \bar{\Delta}^{--}p$, and for events with and without resonance in the final state.

For each bin, we also show σ' for the events without $\bar{\Delta}^{--}$ and those located in the central part of the Dalitz plot. Apart from the $\bar{p}n \to \bar{\Delta}^{--}p$ channel, some weak structure appears in σ' for $M \sim 3.53$ GeV/c^2.

In order to see if the weak structure cannot be due to the particular choice of $\Phi(p_s)$, we have also considered a slightly different expression for the deuteron wave function. Indeed, the expression used is a rather crude approximation for large p_s momentum (i.e., small distance between the bounds p and n in the deuteron). As the constant α largely determines the behavior of $\Phi(p_s)$ for large momenta, we have varied α by 20% in the expression of $\Phi(p_s)$. The last column of Table IV gives the χ^2/n values obtained from the new $\Phi(p_s)$. One observes primarily that the dN'/dP distributions in those ΔM bands which were considered as flat remain flat. We have also verified that the use of the new $\Phi(p_s)$ does not change the structure observed in σ'. In other words, the effect observed in the variation of σ' is not too sensitive to the badly known part of $\Phi(p_s)$.

That σ' for the $\bar{p}n \to \bar{\Delta}^{--}p$ reaction appears to be a decreasing function of M gives some confidence in the

method employed. Indeed, the $\bar{\Delta}^{--}$ resonances in the $\bar{p}n$ c.m. system are all emitted in the forward hemisphere in the c.m. system. Therefore, s-channel resonance is not expected to manifest itself in the $\bar{p}n \to \bar{\Delta}^{--}p$ reaction. In order to see if the structure observed in the $\bar{p}n \to \bar{p}p\pi^-$ reaction may be really due to an s-channel effect, high-statistics $\bar{p}p$ formation experiments in the vicinity of $M \sim 3.5$ GeV would be desirable.

B. Cross Section

Since screening or shadow effects are difficult to estimate in inelastic reactions, we are in fact able to give only the cross section for the $\bar{p}d \to p_s\bar{p}p\pi^-$ process. For p_s momenta greater than 0.1 GeV/c, we found

$$\sigma(p_s > 0.1 \text{ GeV}/c) = 0.41 \pm 0.02 \text{ mb}.$$

To obtain this value, we also took into account the diminution of the total path length due to the various interactions in the chamber. We used a total $\bar{p}d$ cross section of 108 ± 1.5 mb interpolated from the available data.[8,9]

If we take seriously the simplified version of the impulse approximation (i.e., neglecting flux factors, shadow effects, and variation of cross section with M), we can estimate the number of events lost because of small p_s recoil.

Based on the number of events which are in the momentum range of $0.10 < p_s < 0.26$ GeV/c, we obtain

$$\sigma_1(\bar{p}n \to \bar{p}p\pi^-) = 1.50 \pm 0.08 \text{ mb}.$$

This value is comparable in size with

$$\sigma(\bar{p}p \to \bar{p}p\pi^0) = 2.10 \pm 0.23 \text{ mb},$$
$$\sigma(\bar{p}p \to \bar{n}p\pi^-) = 1.77 \pm 0.37 \text{ mb},$$

measured at an $\bar{p}$ incident momentum of 5.7 GeV/c.[10]

A further step can be made by assuming that at high energy the proportion of shadowing or screening effects in each channel is the same as that for the total $\bar{p}d$ cross section.

The expression[11]

$$\sigma_{\text{tot}}(\bar{p}d) = \sigma_{\text{tot}}(\bar{p}n) + \sigma_{\text{tot}}(\bar{p}p) - \delta\sigma,$$

which relates the total cross section on deuterium with those obtained on protons and neutrons, has in the high-energy region a shadow term $\delta\sigma > 0$. One can then consider $\delta\sigma$ as being a consequence of the shadowing of one nucleon by the other inside the deuteron,[12] each of them yielding a $\frac{1}{2}\delta\sigma$ term. Thus $\sigma_2(\bar{p}n \to \bar{p}p\pi^-)$, the cross section on a free neutron, will then be obtained by adding a $\frac{1}{2}\delta\sigma'$ term to the measured value, the $\delta\sigma'$ obeying the condition

$$\delta\sigma = \sum_{\text{all channels}} \delta\sigma'.$$

Taking the simplified form[12] for $\delta\sigma$, i.e.,

$$\delta\sigma = (1/4\pi)\langle r^{-2}\rangle \sigma_{\text{tot}}(\bar{p}n)\sigma_{\text{tot}}(\bar{p}p),$$

one has

$$\delta\sigma' = (1/4\pi)\langle r^{-2}\rangle \sigma_2(\bar{p}n \to \bar{p}p\pi^-)\sigma_{\text{tot}}(\bar{p}p).$$

Using for the mean inverse square of the deuteron radius $\langle r^{-2}\rangle = 0.042 \pm 0.003$ mb^{-1},[8] and $\sigma_{\text{tot}} = 63.6 \pm 1.4$ mb,[9] we obtain

$$\sigma_2(\bar{p}n \to \bar{p}p\pi^-) = 1.68 \pm 0.11 \text{ mb}.$$

The σ_1 and σ_2 values found above are only estimates for the $\bar{p}n \to \bar{p}p\pi^-$ cross section. A better method would consist in calibrating the studied channel by comparing the $\bar{p}n \to \bar{\Delta}^{--}p$ and $\bar{p}p \to \bar{\Delta}^{-}p$ reactions at the same energy. Indeed, the initial states of both reactions have the same $I = 1$ isospin value. Unfortunately the poor statistics available in the $\bar{p}p \to \bar{\Delta}^{--}p$ channel at 5.7 GeV/c do not encourage us to use of this procedure.

ACKNOWLEDGMENTS

We are deeply grateful to the Argonne National Laboratory, which has generously permitted the realization of this experiment. We also thank the ANL High-Energy Group, especially Dr. M. Derrick. It is pleasure to thank Professor H. Filthuth for his support, and Dr. A. Pape for a useful discussion. We are indebted to Professor L. Van Hove, Professor M. Jacob, and Professor E. Gotsman for enlightening discussions.

[8] R. J. Abrams, R. L. Cool, G. Giacomelli, T. F. Kycia, B. A. Leontić, K. K. Li, and D. N. Michael, Phys. Rev. Letters **18**, 1209 (1967).

[9] W. Galbraith, E. W. Jenkins, T. F. Kycia, B. A. Leontić, R. H. Philips, A. L. Read, and R. Rubinstein, Phys. Rev. **138**, B913 (1965).

[10] K. Böckmann *et al.*, Nuovo Cimento **42A**, 954 (1966).

[11] V. Franco and R. J. Glauber, Phys. Rev. **142**, 1195 (1966).

[12] R. J. Glauber, Phys. Rev. **100**, 242 (1955); and in *Lectures in Theoretical Physics*, edited by W. E. Brittin *et al.* (Interscience, New York, 1959), Vol. I, p. 135.